PERGAMON

Available online at www.sciencedirect.com

SCIENCE DIRECT®

Electrochimica Acta 48 (2003) 1169–1191

ELECTROCHIMICA Acta

www.elsevier.com/locate/electacta

Structure, dissolution, and passivation of Ni(111) electrodes in sulfuric acid solution: an in situ STM, X-ray scattering, and electrochemical study

J. Scherer [a], B.M. Ocko [b], O.M. Magnussen [a,*]

[a] *Abteilung Oberflächenchemie und Katalyse, Universität Ulm, Albert-Einstein-Allee 47, D-89069 Ulm, Germany*
[b] *Physics Department, Brookhaven National Laboratory, Upton, NY 11973, USA*

Dedicated to Professor Joachim Walter Schultze on the occasion of his retirement and in recognition of his contribution to electrochemistry and corrosion science.

Abstract

Results of a detailed study of Ni(111) surfaces in air and in sulfuric acid solution (pH 1.0–2.7) by a combination of STM, surface X-ray scattering using synchrotron radiation, and electrochemical techniques are presented. Ni(111) samples, prepared via annealing in H_2 and exposure to air at room temperature, are covered by a smooth three to four layers thick NiO(111) film with parallel (NiO[$1\bar{1}0$]||Ni[$1\bar{1}0$]) and anti-parallel (NiO[$1\bar{1}0$]||Ni[$\bar{1}10$]) in-plane orientation. Electrochemical reduction at potentials ≤ -0.40 $V_{Ag/AgCl}$ results in the formation of a well-defined, oxide-free surface with large terraces, a low surface mobility, and a (1×1) lattice on the atomic scale. X-ray reflectivity data indicate vertical lattice expansion for the topmost Ni layer and a strongly bound sulfate or oxygen species. Active Ni dissolution commences at potentials ≥ -0.25 $V_{Ag/AgCl}$ by a step-flow mechanism, followed by the rapid formation of large three-dimensional etch pits, leading to considerable surface roughening. In situ STM observations of the passive film formation show at potentials ≥ -0.10 $V_{Ag/AgCl}$ the nucleation and growth of an initial 'grainy' phase, which is attributed to a Ni hydroxide, followed by a slower restructuring process. According to our combined STM and SXS data, the resulting steady-state passive film exhibits a duplex structure, with a crystalline, inner NiO(111) layer, consisting of exclusively anti-parallel oriented grains (NiO[$1\bar{1}0$]||Ni[$\bar{1}10$]) which are slightly tilted relative to the substrate lattice, and a porous, probably amorphous hydroxide phase on top. The thickness of the crystalline NiO film increases with potential by 14–17 Å V^{-1}. In addition, structural changes of the oxide film during immersion of Ni samples into the sulfuric acid solution at potentials in the passive range and after emersion from the electrolyte were observed, which indicate the slow conversion of the air-formed into the passive oxide and the (partial) reformation of the air-formed oxide, respectively.
© 2003 Elsevier Science Ltd. All rights reserved.

Keywords: Nickel; Oxidation; Dissolution; Electrochemistry; STM; X-ray diffraction

1. Introduction

The structure and growth of passive films on metal electrodes as well as their influence on corrosion and other electrochemical reactions are and continue to be an extensively studied subject. A concise overview on the current state of passive film research was recently given by Schultze et al. [1], who has contributed important fundamental studies to this field over the last three decades. Here we discuss the case of nickel, which can be considered as a prototypical example of a passive metal. The corrosion of nickel in aqueous electrolytes has been the subject of numerous studies, motivated by the high technological importance of Ni and Ni-containing alloys, such as stainless steels and brasses, as well as by fundamental questions concerning the understanding of the mechanisms of metal corrosion [2–4]. Despite extensive previous studies the microscopic (defect) structure of Ni electrode surfaces and the complex atomic-scale processes underlying metal corrosion and oxidation in an electrochemical environment are considerably less understood than those in Ni gasphase

* Corresponding author. Present address: Institute of Experimental and Applied Physics, Universität Kiel, 24089 Kiel, Germany.

0013-4686/03/$ - see front matter © 2003 Elsevier Science Ltd. All rights reserved.
doi:10.1016/S0013-4686(02)00827-7

terraces and of the monolayer deep pits (an example is marked by circles in Fig. 4b and c), whereas changes in the size or the depth of the large pit at the upper right corner can not be detected. This potential is in good agreement with the onset of a noticeable anodic current in the quasi-stationary polarization curve (see Fig. 1a). The step-flow etching proceeds not uniformly but with pronounced local differences in the dissolution rates. Local redeposition processes, as found e.g. for Cu(100) dissolution in H_2SO_4 [72], were not observed, even at the onset of dissolution. In the further course of the experiment (Fig. 4d), this step flow etching results in the progressive dissolution of the terraces with the etch rate increasing with increasing potential. Due to the non-uniform etch rate along the steps as well as due to merging of monolayer pits with neighboring terrace edges, dents emerge in the steps, resulting in a substantial step roughness with increasing potential and time. At the same time, the deeper pit at the upper right corner of the image starts to rapidly grow laterally and vertically (Fig. 4d). Further 6 min later at the same potential (Fig. 4e), this pit has reached a depth of ~ 20 Å and a diameter of ~ 500 Å. This type of locally enhanced dissolution via three-dimensional pit growth was generally observed in the experiments and leads to an increased surface roughness at higher anodic potentials. As can be seen in the next image (Fig. 4f), obtained 16 min later at -0.12 V, the growth of the large pit has significantly slowed down, however, additional larger 3D pits have evolved on the surface (marked by circles). Interestingly, the 3D pits do not form at bulk defects, such as screw dislocations or inclusions, but on an apparently undisturbed Ni(111) substrate (the influence of surface defects, in particular steps, could not be assessed due to the high step density). In the surface areas surrounding the pits the atomically smooth terraces of the Ni(111) surface remain visible, indicating that these areas are free of the passive film. Consequently, these areas are either still in the active state or only covered by an adsorbate layer. At more positive potentials no stable STM images could be obtained in this series, which was a general problem of the experiments in the regime of high dissolution rates.

These observations, i.e. a step-flow mechanism in the entire range of dissolution and the parallel formation of 3D pits at more anodic potentials, were supported by other in situ STM experiments on Ni(111) in 0.05 M H_2SO_4. In addition, these measurements revealed a dependence of the active Ni dissolution on the rate of potential increase: In experiments where the potential was increased at a very low rate, such as in that shown in Fig. 4, dissolution usually commenced at potentials in the range -0.25 to -0.20 V, whereas at higher rates of potential increase marked dissolution was often observed only at more anodic potentials and frequently coincided with passive film formation (see below). In a similar way, the initiation potential and the kinetics of the 3D pit formation and growth, which is the dominant dissolution mechanism at more anodic potentials, also varied from experiment to experiment. Finally, also the spontaneous slow down or complete stop of 3D pit grow, described above, were observed in other experiments, suggesting (re-) passivation of these highly active areas. A more detailed discussion of the Ni dissolution behavior, in particular of the unusual pitting of the oxide-free surface, will be given in Section 4.3.

3.2.4. Passive film formation on Ni(111) in 0.05 M H_2SO_4

The formation of the passive film on Ni(111) in 0.05 M H_2SO_4 was studied by similar series of STM images, recorded during the stepwise increase of the potential from the stability range of the reduced metal into the passive range. To prevent surface roughening due to anodic dissolution the potential was increased at a higher rate (see above). As an example, four consecutive images from a series where the potential was increased from -0.40 to 0.05 V by 50 mV every 6 min are shown in Fig. 5. Up to the image in Fig. 5a, obtained 180 s after the potential step to 0.05 V, no significant changes in the topography had been observed. In the subsequent image (Fig. 5b), however, sudden drastic changes in surface structure are found. During the first ~ 20 s (Fig. 5b, upper half), the observations indicate the removal of an entire monolayer via step-flow dissolution. At later times the surface roughness increases (Fig. 5b, bottom half), suggesting rapid metal dissolution via 3D pit growth. The formation of these 3D pits seems to occur favorably at the location of the monolayer deep pits visible in the center of the previous image (Fig. 5a). Parallel to these dissolution processes, small islands with diameters of 20–100 Å and apparent heights of 1–2 Å (see also cross-section in Fig. 5e) emerge, which apparently nucleate preferentially along the Ni steps. With time the number of these islands increases continuously until the surface is entirely covered at $t = 180$ s. A similar grain-like morphology was reported in the in situ STM studies of passivated Ni(111) in H_2SO_4 solution by Zuili et al. [33,36]. Following their interpretation, this morphology is attributed to the amorphous outer part of the passive layer consisting of a Ni oxide/hydroxide phase. This view is also supported by the simultaneously measured electrochemical current, which exhibited a sharp drop parallel to these morphological changes. In the further course of the experiment (Fig. 5c and d), a coarsening of the islands is observed, in which the grain-like morphology is gradually transformed into a highly stepped structure characterized by terraces with widths of 20–60 Å, separated by parallel oriented steps. The terraces are tilted by 3–15° with respect to the bare Ni(111) surface visible in Fig. 5a (see cross-section in Fig. 5b). Again,

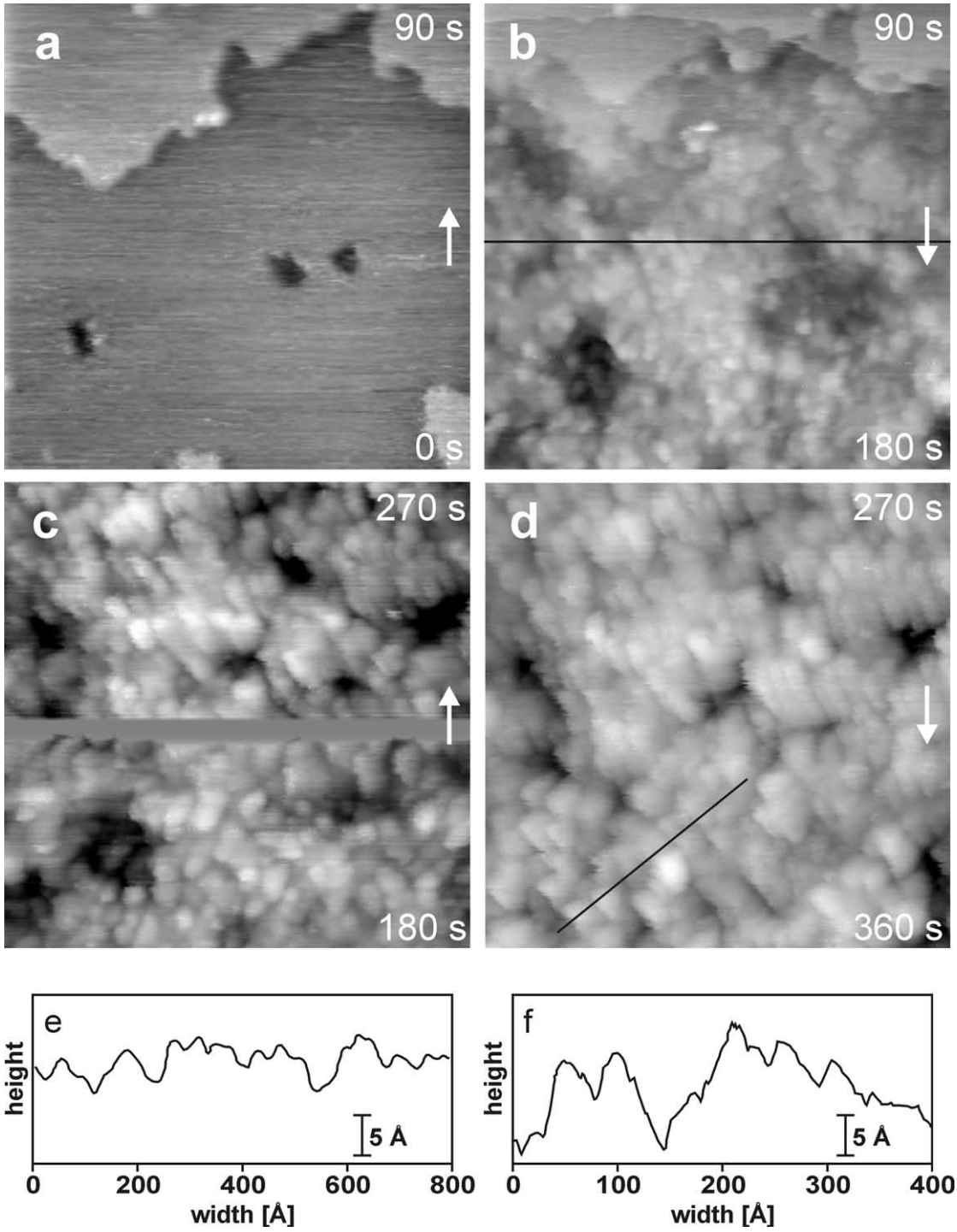

Fig. 5. Series of in situ STM images (800 × 800 Å^2, $U_{bias} = -310$ mV, $I_t = 2.51$ nA) showing time-dependent morphological changes during passive layer formation at 0.05 V in 0.05 M H_2SO_4. (a) Reduced Ni surface at $t = 0$ s, recorded after potentiostatic reduction at cathodic potentials and a subsequent, fast stepwise increase of the potential. (b–d) Subsequent images, recorded at (b) $t = 180$ s, (c) $t = 90$ s, and (d) $t = 270$ s (scan direction indicated by arrows). The gray stripe in (c) is an artifact caused by a readjustment of the z-scale. (e) And (f) cross-sections at the positions of the black lines in (b) and (d), which illustrate the increased roughness and the formation of the stepped morphology.

these observations are in good agreement with previous STM observations of the passive film on Ni(111) surfaces [32,33,36,48,49], where such stepped morphologies were attributed to the inner (crystalline) NiO(111) part of the passive film (for a more detailed discussion see Sections 4.2 and 4.3). Whereas the grainy structure could be always imaged after passivation, stepped structures were only observed in some of the experiments. This may be caused by differences in the tunneling conditions (U_{bias}, I_t, and/or state of the tip),

which reportedly can determine whether the stepped morphology of the crystalline NiO or the grain-like morphology of the outer hydroxide layer are imaged [33,36], or by differences in the tip resolution.

In the STM experiments passivation was often accompanied by severe instabilities in the imaging, either due to high local dissolution rates prior to passive film formation or, more likely, due to the formation of insulating or semiconducting oxide particles. Furthermore, although the general features of passive film formation were the same, noticeable differences in the passivation potential (between −0.05 and 0.10 V) and in the kinetics of the processes associated with passivation were observed. These effects might be related to changes in pH in the rather small STM cell. For direct comparison with the X-ray results, also experiments were performed in which the surface was passivated after reduction by potential steps into the passive regime (0.30–0.90 V). In this case, however, no reproducible, stable imaging of the passive film was possible, despite a wide variation of the tunneling conditions. This probably has to be attributed to the formation of a thicker and therefore (locally) less conductive film at more positive potentials (see Section 3.3) as well as to the considerable surface roughening caused by the anodic dissolution during passive layer formation in 0.05 M H_2SO_4 solution (see above). Due to the lower pH these Ni dissolution processes are much more pronounced as in the previous in situ STM studies, where observation of the passive film was possible [33,36]. The latter studies also revealed an increase in roughness with more anodic passivation potential, which may explain why samples could be imaged after passivation at ∼ 0.00 V, but not after passivation at more anodic potentials (≥ 0.30 V).

3.2.5. Structure of air-formed oxide on Ni(111) after immersion in 0.05 M H_2SO_4

In addition to in situ STM experiments on reduced Ni, the surface structure and morphological changes of air-formed oxide covered Ni(111) electrodes in 0.05 M H_2SO_4 were studied in experiments, where the annealed samples were directly immersed under potential control at potentials in the passive range (i.e. without prior reduction). The typical surface morphology observed under these conditions is illustrated by the image shown in Fig. 6a, which was acquired 90 min after immersion at 0.50 V. On the image large terraces covered by a high density of pits and some islands are visible. The terraces were usually separated by steps with heights of 2.0 ± 0.2 and 2.5 ± 0.2 Å, which can be attributed to monolayer NiO(111) oxide and Ni(111) substrate steps, respectively. The pits usually exhibited diameters of 20–100 Å and apparent depths of about 2.5 or 5.0 Å (Fig. 6b), i.e. one or two NiO(111) layers. They seem to be preferentially localized at the steps of the NiO film. The density

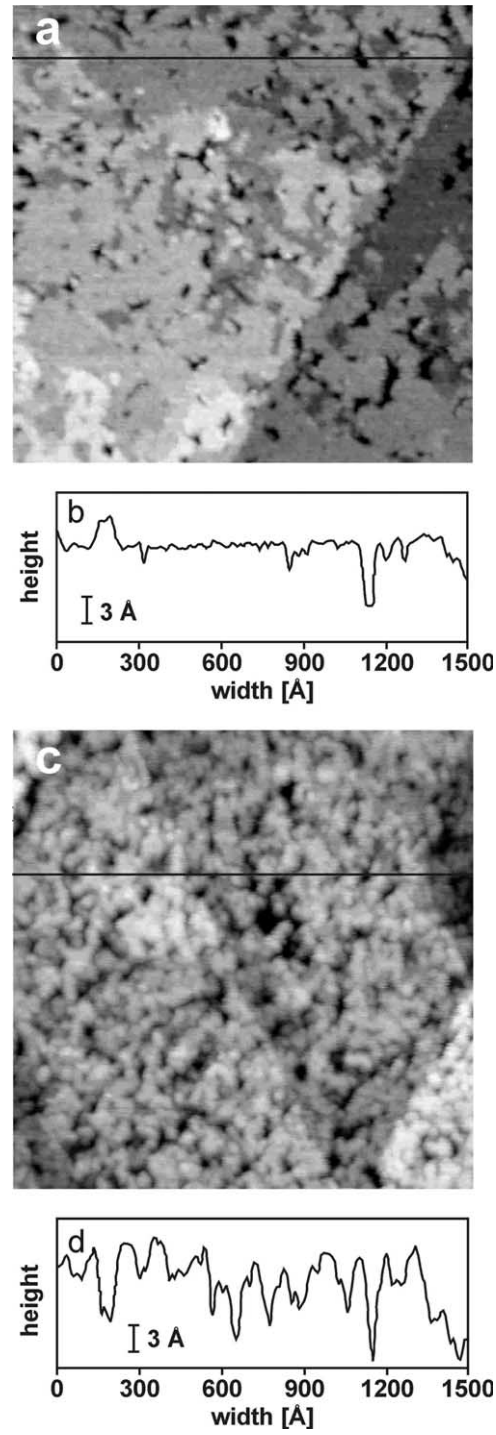

Fig. 6. (a, c) In situ STM images (1500 × 1500 Å^2) and (b, d) corresponding cross-sections of Ni(111) surfaces after direct immersion of air-formed oxide into 0.05 M H_2SO_4 at 0.50 V: (a, b) Ni surface after ∼90 min at 0.50 V ($U_{bias} = -800$ mV, $I_t = 0.4$ nA). (c, d) Different location on the same sample after ∼200 min at 0.50 V ($U_{bias} = -900$ mV, $I_t = 1$ nA).

of the pits (∼ 5–7 × 10^{11} cm^{-2}) is much higher than that observed in the ex situ STM experiments of the air-formed oxide in air (see Fig. 2), which is attributed to pit formation via local oxide dissolution (e.g. at defects in

the initial air-fomed oxide) after contact with the electrolyte solution. Such pits were already found in the first images (~ 10 min after immersion), demonstrating that at least a part of them is formed already after very short times. Overall, the surface morphology is rather smooth compared with that formed by passivation of reduced samples, which is also indicated by the X-ray reflectivity data (see below). This suggests that the air-formed oxide effectively blocks the anodic dissolution.

For longer immersion periods at constant potential gradual changes in the surface morphology are observed on a timescale of hours, resulting in an increasingly grainy appearance (Fig. 6c). Generally, the surface is totally covered by grains after 120–180 min. The lateral grain sizes are between 20 and 100 Å, i.e. of similar dimensions as those observed during passive layer formation (see above). The pits formed in between the grains in the earlier stages remain visible, but exhibit now depths up to 10 Å, suggesting a thickening of the oxide film and/or further dissolution via pit growth (Fig. 6d). Following the assignment by Zuili et al. [33,36], the formation of the grainy structure might be caused by the precipitation of a (possibly amorphous) hydroxide layer on top of the crystalline oxide and/or a gradually increasing degree of hydration of the upper oxide layers.

3.3. X-ray scattering measurements

3.3.1. Passive film structure in 0.05 M H_2SO_4

First, the main results of our recent in situ X-ray scattering study on the structure of the passive film formed on reduced Ni(111) electrodes by passivation in 0.05 M H_2SO_4 (pH 1.0) at 0.50 V [51] are summarized. The corresponding geometry in reciprocal space is shown schematically in Fig. 7. Here circles and bold lines indicate Bragg peaks and crystal truncation rods (CTRs) of the Ni(111) substrate, respectively, whereas the oxide diffraction peaks are indicated by triangles. For the passive oxide broad peaks are observed at ($a^*_{NiO}h'$, $a^*_{NiO}k'$, $c^*_{NiO}(2h'+k'+3l')$) with h', k', $l'=0$, ±1, ±2, ... (a^*_{NiO} and c^*_{NiO} are given in units of a^*_{Ni} and c^*_{Ni}, respectively). This diffraction pattern corresponds to a (111)-oriented fcc-NiO phase with a well-defined antiparallel in-plane orientation with respect to the substrate (NiO[1$\bar{1}$0]||Ni[$\bar{1}$10]), i.e. the ABC Ni(111) stacking sequence is followed by BAC NiO(111) fcc-stacking. We attribute this phase to the inner crystalline part of the passive layer. Transverse scans across the first- (Fig. 8a,b) and second-order (Fig. 8c) peak positions (a^*_{NiO}, a^*_{NiO}, 0), (a^*_{NiO}, 0, c^*_{NiO}), and (a^*_{NiO}, 0, c^*_{NiO}) show the characteristic threefold symmetric diffraction pattern of the antiparallel oriented NiO with first order peaks (denoted by 'AP') at every 120° and second order peaks at every 60° (solid lines; the data for the in-plane peak at (a^*_{NiO}, c^*_{NiO}, 0) were recorded at

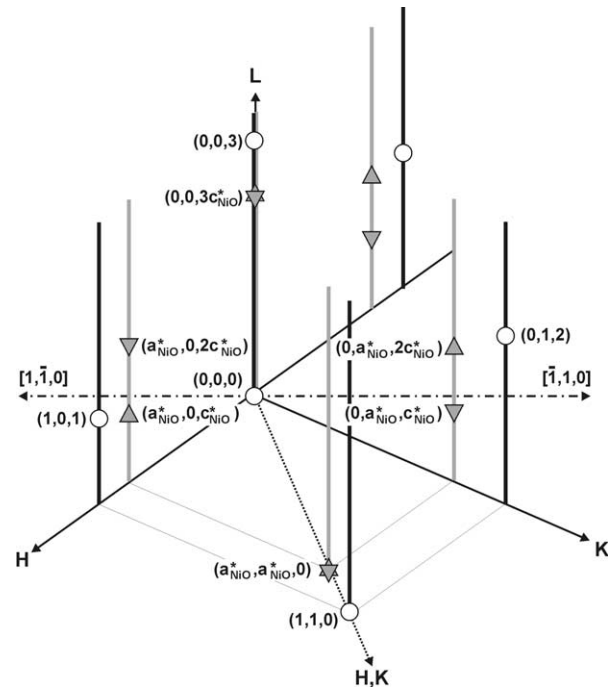

Fig. 7. Schematic diffraction pattern showing the reciprocal space positions of the Ni(111) substrate peaks (O), the Ni(111) CTRs (black bold lines), and the peaks of the parallel (△) and antiparallel (▽) NiO phase (☆ indicates that the NiO peak positions overlap).

$L=0.2$). The absence of peaks located inbetween the maxima indicates that NiO(111) phases with different in-plane orientations than the antiparallel oriented NiO do not exist in significant amounts. In particular, no first-order peaks at the 60° rotated positions ('P'), indicative of a parallel oriented NiO phase (see below), are found for the passive film. Furthermore, despite extensive searches, in none of the experiments a diffraction pattern characteristic of a fcc-NiO with different surface-normal orientation or of other crystalline Ni oxide/hydroxide phases, e.g. a $Ni(OH)_2$ phase, was found.

From the peak profiles along the radial and surface-normal directions [51] (see also Fig. 10a,b), the (three-dimensional) passive film lattice structure in 0.05 M H_2SO_4 solution could be obtained in situ with high precision. Table 1 summarizes the structural parameters for passive oxide formed by a potential step from −0.40 to 0.50 V [51]. According to these data, the oxide is composed of NiO(111) crystallites with average diameters < 100 Å, suggesting a high number of Ni nuclei during passive film formation, and about five to six layers thickness. The in-plane spacing of the passive oxide is within the experimental error identical to that of bulk NiO, however, the surface-normal spacing is significantly expanded with respect to that of bulk NiO. Since only the average vertical expansion is obtained from the position of the peak maximum, it is possible that only a fraction of the NiO layers is

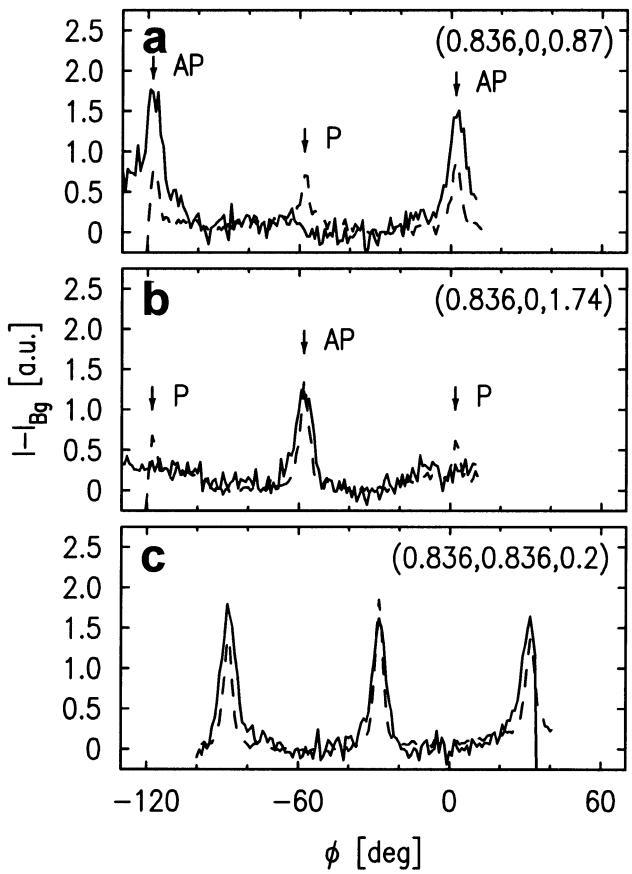

Fig. 8. Transverse peak profiles through the three low-order peak positions (a–c) for passive oxide on Ni(111), obtained in situ at 0.50 V in 0.05 M H_2SO_4 (solid lines). The exact positions are given in brackets. Previously, the passive film was formed by a potential step to 0.50 V. For comparison corresponding profiles for air-formed oxide, obtained ex situ under N_2 (dashed lines), are shown. The positions expected for the parallel and antiparallel NiO phases are marked with arrows and denoted with P and AP, respectively.

expanded (by an even larger amount), whereas the remaining fraction exhibits a bulk-like spacing. As will be discussed in Section 4.5, this lattice expansion might be explained by (partial) hydration and/or hydroxylation of NiO. Detailed mesh scans of the peaks revealed that the NiO crystallites are tilted relative to the Ni(111) substrate with a broad angular dispersion of the tilt angle centered at about $\pm 3.3°$ [51], which is in agreement with previous STM results [33,36,48,49].

In the following, new data on potential-dependent changes of the oxide film structure are presented. Two types of experiments were performed: First, similar as in our previous study [51] passive films were formed on reduced samples by a single potential step to a potential in the passive range (method I). Second, after forming an initial passive film by a potential step from −0.40 to 0.30 V the potential was successively increased in steps of 0.10 V and the passive film structure was studied after each potential step (method II). In all of these experiments only the antiparallel oxide phase was observed, indicating that this orientation is preferred in an electrochemical environment, independent of the potential or of the method by which the passive oxide is formed. The measured in-plane and surface-normal peak positions were identical with the values obtained after passivation at 0.50 V, i.e. the NiO lattice constants are independent of the formation conditions. Furthermore, the relative transversal and lateral widths of the different diffraction peaks qualitatively indicate a similar tilt of the oxide lattice [51]. A quantitative description of the potential-dependence of the oxide structure by detailed mesh scans, however, in particular of the tilt and tilt distribution, was not possible due to beam time constraints.

In the experiments by method I, where the oxide layer was formed by single potential steps (to 0.30, 0.50, 0.70, or 0.90 V), the radial peak widths tend to increase with increasing passivation potential. This corresponds to a decrease in the in-plane domain size of the passive oxide with passivation potential, indicating an increase in the number of oxide nuclei. In contrast, in experiments employing method II the radial in-plane peak widths remained approximately constant. In this case the in-plane domain size most likely is determined by the saturation density of oxide nuclei during the initial

Table 1
Overview of the structural parameters of passive oxide formed on Ni(111) by a potential step to 0.50 V in 0.05 M H_2SO_4 compared with those for air-formed oxide on freshly H_2-annealed Ni(111) [51]

	Passive oxide	Air-formed oxide
Surface-normal orientation	NiO[111]||Ni[111]	NiO[111]||Ni[111]
In-plane orientation (stacking sequence)	NiO[1$\bar{1}$0]\|\|Ni[$\bar{1}$10] (**CBA**BCA)	NiO[1$\bar{1}$0]\|\|Ni[$\bar{1}$10] and NiO[1$\bar{1}$0]\|\|Ni[1$\bar{1}$0] (**CBA**CBA and **CBA**BCA)
Tilt	Yes	No
In-plane spacing a_{NiO} (Å)	2.959 ± 0.004	2.998 ± 0.004
In-plane lattice expansion relative to bulk NiO(111) (%)	0.1	2.5
Surface-normal spacing c_{NiO} (Å)	7.50 ± 0.01	7.41 ± 0.01
Surface-normal lattice expansion relative to bulk NiO(111) (%)	3.7	1.1
Average in-plane domain size (Å)	80	70–120

passive film formation (i.e. during the potential step from −0.40 to 0.30 V) and does not change during the subsequent potential steps.

As mentioned above, the oxide lattice structure, the tilt angle, and the tilt distribution seem to be independent of potential and can be safely assumed to remain unchanged after formation of the initial oxide film. Consequently, the only potential-dependent changes which have to be considered are changes in the thickness of the crystalline oxide film, i.e. the vertical growth or thinning of the inner passive layer with potential. Assuming that all other lattice parameters are independent of the potential, the oxide thickness can be easily calculated from the width of the NiO diffraction peaks along the surface-normal direction via the Debye–Scherrer formula. Indeed, a pronounced dependence of the oxide thickness on the potential was obtained from the L-widths of the peaks at (0, a^*_{NiO}, c^*_{NiO}) and (a^*_{NiO}, 0, 2, c^*_{NiO}) (Fig. 9a,c). Measurements of the thickness of passive films formed by method II in 0.05 M H_2SO_4, pH 1.0 (Fig. 9b) and in 2.5 mM H_2SO_4/0.05 M Na_2SO_4, pH 2.7 (Fig. 9d) show an approximately linear increase of the oxide thickness with potential between 0.30 and 0.80 V with slopes of (17±2) and (14±2) Å V^{-1}. According to these data the thickness of the (crystalline) oxide at 0.50 V is about 16 and 13 Å for the passive film in 0.05 M H_2SO_4 and 2.5 mM H_2SO_4/0.05 M Na_2SO_4, respectively. (due to an incorrect subtraction of the considerable nonuniform background in the in situ SXS experiments a higher passive film thickness of 24 Å was reported in Ref. [51] for passivation at 0.05 V in 0.05 M H_2SO_4). The thicknesses reported here are based on a detailed reanalysis of that data, where background data obtained at $\phi = \phi_{peak} \pm 7°$ (see Fig. 7) was taken into account). Interestingly, the oxide thickness decreases after the potential step to 0.90 V, which might by rationalized by changes of the passive film due to the onset of transpassive dissolution.

3.3.2. Dependence of the oxide film structure on the environment

SXS measurements were also utilized to study the structural changes in the oxide film on Ni(111) during the different stages of the sample preparation, i.e. (i) after H_2 annealing and exposure to air, (ii) after reduction in 0.05 M H_2SO_4 at potentials ≤ −0.40 V, (iii) after immersion at potentials in the passive range, (iv) after passivation by potential steps (see above), and (v) after emersion of passivated samples from the electrolyte. In Fig. 10 characteristic surface-normal (Fig. 10a) and radial peak profiles (Fig. 10b) at (a^*_{NiO}, 0, 2, c^*_{NiO}) are shown, which illustrate the pronounced changes of the NiO diffraction peaks under these varying conditions. As shown previously [51], the air-formed oxide on freshly annealed samples (Fig. 10a, profile A and Fig. 8a,b) differs considerably from the passive film. It is composed of both parallel (peak at $L \sim 0.8$) and antiparallel (peak at $L \sim 1.6$) oriented NiO

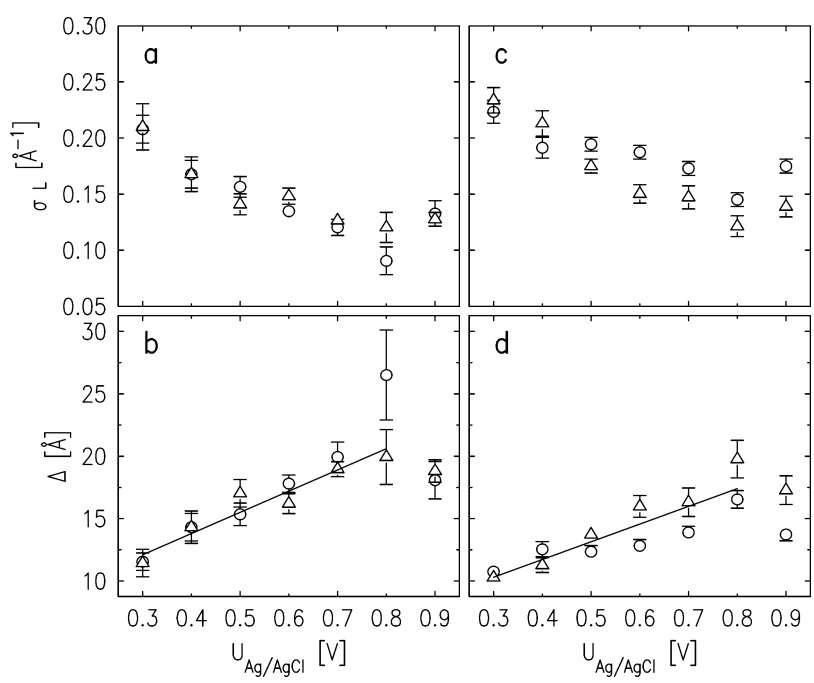

Fig. 9. Potential-dependent (a,c) L-widths and (b,d) thickness of the passive oxide on Ni(111) in (a,b) 0.05 M H_2SO_4 (pH 1.0) and (c,d) 2.5 mM H_2SO_4/0.05 M Na_2SO_4 (pH 2.7). Circles and triangles denote values calculated from the peaks at (0, a^*_{NiO}, L) and (a^*_{NiO}, 0, L), respectively. In these experiments the potential was increased in steps of 0.10 V after formation of the initial oxide by a potential step from −0.40 to 0.30 V. Solid lines in (b,d) correspond to linear fits of the data and give slope of (17±2) Å V^{-1} at pH 1.0 and (14±2) Å V^{-1} at pH 2.7 for the potential-dependence of the oxide thickness.

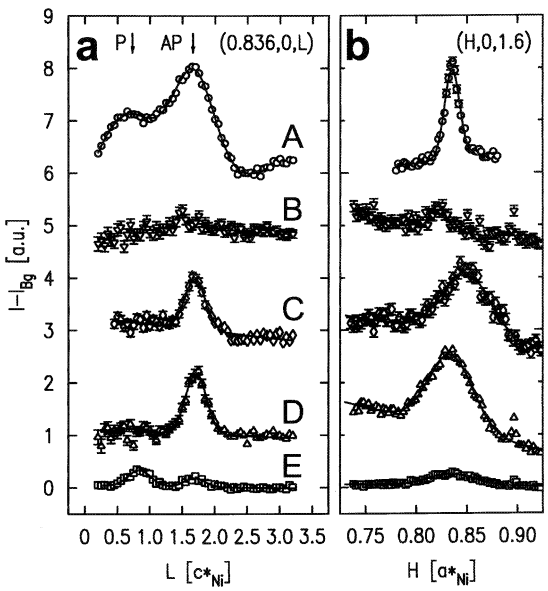

Fig. 10. Dependence of the NiO structure on the environment illustrated by surface-normal (a) and radial (b) peak profiles at one low-order peak position (vertically shifted by 1, 3, 4.5, and 6 arbitrary units, for better visibility). From top to bottom the curves show peak profiles of samples (A) in air, covered by air-formed oxide, (B) in 0.05 M H_2SO_4 after 15 min cathodic polarization at −0.60 V, (C) in 0.05 M H_2SO_4 after ∼360 min immersion under potential control at 0.50 V, (D) in 0.05 M H_2SO_4 after reduction and subsequent passivation by a potential step to 0.70 V, and (E) in air, (a) ∼30 min and (b) ∼60 min after emersion from 0.05 M H_2SO_4. Solid lines represent Gaussian fits of the peak profiles, the positions corresponding to the parallel and antiparallel NiO phases are marked with arrows and denoted by P and AP.

domains, which are not tilted relative to the Ni substrate. The peaks along L are rather broad, indicating an oxide film thickness of 7–10 Å. The structural parameters of the air-formed oxide are included in Table 1. After immersion at −0.40 V and subsequent reduction by 15 min polarization at −0.60 V in 0.05 M H_2SO_4 (Fig. 10, profile B) the oxide peaks have disappeared (the residual structures in the scans, in particular the small peak at $H = 0.82$, are caused by the nonlinear background in the in situ experiments), indicating complete removal of the NiO film.

In alternative experiments Ni surfaces covered by an air-formed oxide were immersed (without prior reduction) under potential control at potentials in the passive range. As an example of the NiO phase formed under these conditions the profiles C in Fig. 10 are shown. They were obtained after immersion into 0.05 M H_2SO_4 solution at 0.50 V and 360 min exposure to the solution at this potential. In contrast to the ex situ data on the air-formed oxide only peaks at ($a^*_{NiO}h'$, $a^*_{NiO}k'$, $c^*_{NiO}(2h'+k'+3l')$) with h', k', $l' = 0, \pm1, \pm2, \ldots$ (i.e. only at $L \sim 1.6$ in Fig. 10a), corresponding to the antiparallel orientation, are observed whereas peaks corresponding to the parallel-oriented NiO phase are absent or present only in very small amounts. Hence, the oxide structure under these conditions is very similar to that of the passive film formed on reduced samples by a potential step to the same potential (Fig. 10, profile D). Furthermore, also the widths of the peaks in the L- and H-scans of profiles C are almost identical to those in the profiles D, but strongly differ from those of the air-formed oxide (profiles A). These observations indicate that upon immersion in the passive range the air-formed oxide is transformed into an oxide phase with similar oxide thickness, lattice parameters (including orientation and tilt), and average domain size as those of the passive film formed on the oxide-free surface by a potential step. This transformation is attributed to the continuous dissolution and reformation of the oxide in the passive range [52,53] (see Section 4.4).

In addition, the structure of electrochemically formed passive films was studied after emersion from the electrolyte. In these experiments, the samples were passivated in the electrochemical or SXS cell, emersed, rinsed with ultrapure water and dried in a N_2-stream. In subsequent ex situ SXS measurements in a N_2 atmosphere (Fig. 10, profile E), started ∼10 min after emersion, similar peak intensities for the parallel and the antiparallel orientation were found, whereas in in situ SXS measurements performed directly before emersion only the antiparallel-oriented oxide was present. Although the intensities for emersed samples are always significantly lower (here by a factor of 2–3), the peak widths in L are very similar prior to and after emersion (here 0.165 and 0.163 $Å^{-1}$ for the peak at $L \sim 1.6$), suggesting that the thickness of the crystalline part of the passive film does not change significantly during emersion. Interestingly, a similar peak width, i.e. a similar oxide thickness, is also found for the parallel-oriented phase, which is formed in the emersion process. Furthermore, almost identical radial peak widths for the oxide film are observed in situ and ex situ after emersion (here 0.063 and 0.067 $Å^{-1}$, respectively). The significantly lower peak intensities after emersion are surprising, since a similar film thickness should correspond to a similar amount of NiO. They might be explained by a less defined oxide structure, e.g. a large fraction of differently oriented or tilted NiO grains or the presence of other oxide/hydroxide phases on the surface. Finally, it is noted that all these structural parameters clearly differ from those of the oxide formed by exposure of H_2-annealed samples to air. As will be discussed in greater detail in Section 4.4, these observations can be rationalized (i) by partial dissolution of the passive film during emersion and subsequent reformation of the oxide film due to exposure to (moist) air and/or (ii) by conversion of the hydroxide/hydrated oxide component of the passive film.

3.3.3. X-ray reflectivity measurements

Parallel to the in-plane diffraction experiments specular X-ray reflectivity measurements were performed. In Fig. 11 specular X-ray reflectivity data on the air-formed oxide obtained ex situ under N_2 (top, open circles) as well as in situ data on the air-formed oxide after immersion in 0.05 M H_2SO_4 (center, squares), and after cathodic reduction of the air-formed oxide in 0.05 M H_2SO_4 (bottom, triangles) are presented. The reflectivity R is plotted as a function of L in units of c^*_{Ni}, the reciprocal surface-normal lattice spacing of Ni(111). For clarity the plots are shifted along the y-axis (center $\times 10^3$, top $\times 10^7$) and the error bars are omitted. Obviously, the curves clearly differ in between the Bragg reflections of the Ni(111) substrate at $L = 3$ and $L = 6$, however, in all three cases measurable intensity is obtained in the entire L range, indicating that the surface is relatively smooth on the atomic scale.

The ex situ reflectivity profile of the air-formed oxide exhibits at small L two broad peaks with maxima at $L \sim 0.8$ and $L \sim 1.6$. Although qualitatively similar curves were obtained, the comparison of different experiments revealed slight differences in the position and separation of these peaks. The intensity modulations at small L are characteristic of an overlayer with different (absolute) electron density than the substrate

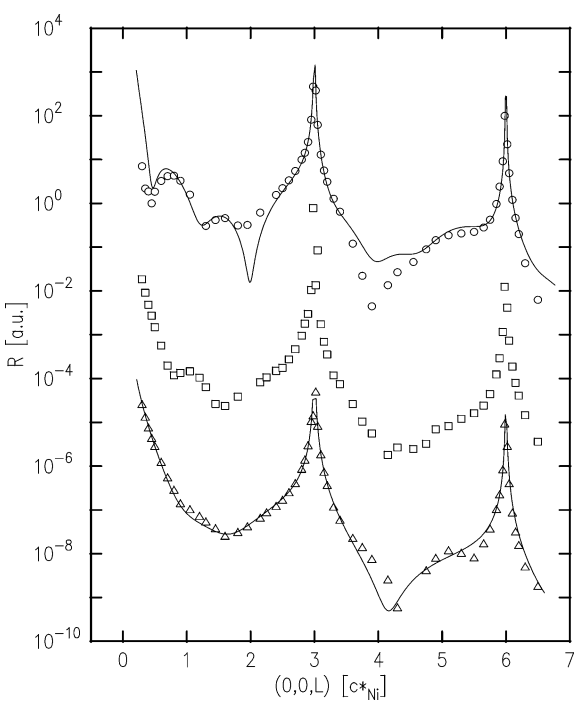

Fig. 11. Specular X-ray reflectivity curves for air-formed oxide on Ni(111) obtained ex situ ($\times 10^7$, top, circles), in situ after immersion into 0.05 M H_2SO_4 at -0.40 V ($\times 10^3$, center, squares), and in situ at -0.40 V (bottom, triangles) after previous reduction of the air-formed oxide by cathodic polarization at -0.60 V. In addition, calculated reflectivity profiles are displayed for air-formed oxide ($\times 10^7$, solid line, top) and for reduced samples (solid line, bottom).

and can be attributed to the presence of the NiO layer. From the modulation period (peak separation) a the thickness Δ of the overlayer was calculated using $\Delta = 2\pi/a$, which yields (depending on the particular experiment) a thickness of 7.0–10.3 Å for air-formed oxide. This value agrees well with the oxide thickness determined from the width of L-scans and corresponds to three to four layers of NiO(111).

For a more quantitative description, a model was used where the oxide was described by a homogeneous NiO(111) multilayer on the Ni(111) substrate. Variable parameters were the density, thickness, and (Gaussian) roughness of the oxide layer, the surface-normal NiO(111) lattice distance, the average displacement amplitude (Debye–Waller factor) of the Ni^{2+} and O^{2-} ions in the oxide lattice, and the spacing between NiO and the Ni substrate. The best description of the reflectivity data in Fig. 11 (Fig. 11, top, solid line) was obtained for a 7.0 Å thick oxide with a small surface roughness of 0.15 Å (corresponding to three complete NiO layers with a 30% partially filled NiO layer on top), a 13% reduced layer density as compared with bulk NiO, and a 0.5% surface-normal expansion of the oxide lattice, which is in good agreement with the diffraction and STM data. The remaining discrepancies between the fit and the experimental data can be attributed to structural features not accounted by the model, e.g. the cluster-like B-type islands observed by STM.

Reflectivity curves for air-formed oxide immersed at -0.40 V without previous reduction at more negative potentials are shown in the center of Fig. 11 (filled circles). According to in-plane diffraction data the air-formed oxide is only slowly chemically dissolved and/or reduced at this potential [51]. Around $L = 1$ a broad peak is visible, indicating the presence of a NiO layer with a considerably smaller thickness than that of the air-formed oxide. Unfortunately, the oxide structure changed considerably during the 60 min required for obtaining the complete reflectivity curve (a second curve recorded directly after resembled that of reduced Ni), so that modeling of the data was not possible. Nevertheless, the data suggest qualitatively that the reduction (at least at -0.40 V) proceeds by a gradual, rather homogeneous decrease in oxide film thickness rather than by dissolution of successive individual oxide grains via a nucleation and growth mechanism. A typical in situ reflectivity curve for cathodically reduced Ni(111) electrodes is shown at the bottom of Fig. 11 (triangles). In this experiment the air-formed oxide was reduced by 15 min polarization at -0.60 V and subsequently characterized at -0.40 V, to avoid H_2-evolution during the X-ray measurements. In contrast to the reflectivity of the air-formed oxide no peaks are visible between $L = 0$ and 2. This indicates that the oxide overlayer is completely removed after reduction, which is in accordance with the diffraction and STM results (see above).

Nevertheless, the curve clearly deviates from that of an ideally terminated Ni(111) surface. In particular, a pronounced minimum at $L = 4.3$ followed by a broad shoulder around $L = 5.1$ is visible, which was found to be characteristic of reduced samples.

To determine the origin of these features, the reflectivity data were fitted to a quantitative model of the interface, similar to that used by Wang et al. for the description of the Au-electrolyte interface [62]. In this model the surface-normal layer spacing, the atomic displacement amplitude (Debye–Waller factor), and the density of the topmost Ni layer was allowed to vary. The latter also allows to account for the monolayer deep pits observed by STM (see Section 3.2). Furthermore, a chemisorbed adlayer on top of the Ni surface and an adjacent, outer water layer was included in the model (the presence of one or two layers of water was also required for the description of reflectivity data on Au and Ag [62,73]). As possible adsorbates oxygen species, such as O, OH, OH_2 and/or SO_4^{2-}/HSO_4^- (a discrimination between those species is not possible due to the very similar electron density), were considered. However, since these adsorbate species are weak scatterers compared with Ni, the main contribution of the reflected intensity is expected to result from the Ni lattice. Within this model the characteristic features of the experimental data, in particular of the shoulder around $L = 5.1$, could solely be reproduced if the topmost Ni-layer was only partially occupied (corresponding to the presence of pits in the surface) and its spacing to the underlying Ni substrate was slightly expanded relative to bulk Ni. The best least-square-fit of the experimental data (Fig. 11, bottom, solid line) was obtained using an 80% occupied Ni surface layer with a 6% expanded surface-normal spacing, covered by a full monolayer of chemisorbed oxygen 1.25 Å above the topmost Ni layer. In addition, a rather broad layer composed of O^{2-} (or H_2O) and located 2.40 Å above the Ni surface layer was used. Although this choice of parameters is not unambiguous and similar fits could be obtained with slightly different parameter sets, the model provides clear (semi) quantitative results on the interfacial structure, i.e. an only partial occupation of the topmost Ni-layer, a slight expansion of the spacing between first and second Ni layer, and the presence of an adsorbate.

4. Discussion

4.1. Ni(111) surface structure in air

We first briefly discuss the initial structure and morphology of the Ni(111) surface prior to immersion into the electrolyte, which is an important prerequisite for an understanding of the in situ results. As shown by the STM and SXS data, after annealing in H_2 and oxidation in air at room temperature, the Ni(111) samples exhibited rather well-defined surfaces. Obviously, the annealing procedure results in extended, atomically smooth terraces on the metallic Ni. After exposure to air an uniform, epitaxial NiO(111) film is formed on this substrate, which exhibits a similar morphology as that found in previous STM studies in air [33,36,48,49] and in an UHV–STM study of Ni(111) oxidation [74]. Highly stepped morphologies, which are apparently characteristic of tilted oxide overlayers on Ni [33,36,48,49,75], are absent, in agreement with our previous SXS results, where an untilted growth of the air-formed oxide on the Ni(111) surface was found [51]. According to the SXS data the average oxide thickness is three to four layers, which confirms previous results [65,74,76–78]. During the growth of the air-formed oxide film each Ni layer is converted into 1.4 ML NiO due to the 70% lower density of Ni atoms in NiO as compared with that in Ni metal. Starting from a smooth Ni substrate, this necessarily results in the formation of an only partially filled NiO layer at the oxide surface and/or the oxide/metal interface, which can explain the presence of the (A-type) NiO(111) islands observed by STM. As a consequence, local variations in the oxide thickness of one to two layers are expected. Furthermore, the experimental results suggest that the entire oxide film up to the surface layer crystallizes in a (111)-oriented NiO lattice. Due to the rather high humidity in air, the NiO(111)-(1 × 1) surface is probably stabilized by a OH-termination [74,79–82]. In addition to the NiO phase the STM images indicate the presence of an additional Ni-oxide or -hydroxide phase (B-type islands) The formation of this probably amorphous phase might be induced by the high humidity, as suggested by the observation of similar structures on top of passive films on Ni(111), which were assigned to Ni-hydroxide [33,36]. The mechanism of the oxide film growth, although not explicitely studied here, most likely is similar to that found under UHV conditions, where the nucleation of oxide islands followed by lateral island growth was inferred [5]. The small NiO domain size, which is much smaller than the size of the Ni terraces indicates a high (homogeneous) nucleation density, whereas the observation of coalescing A-type islands suggests island growth at the perimeter.

4.2. Surface structure of reduced Ni(111)

In accordance with previous electrochemical results [22], the in situ STM and SXS measurements show that the air-formed oxide on Ni(111) can be completely reduced by cathodic polarization in 0.05 M H_2SO_4, resulting in metallic Ni electrode surfaces with extended, atomically smooth terraces, which are separated by monolayer steps. In contrast to Ni(111) surfaces under

UHV conditions, which exhibit after several sputtering and annealing cycles smooth steps and defect-free terraces [74], the terrace edges on reduced Ni(111) surfaces are relatively rough and on the terraces characteristic monolayer deep pits are found, similar as reported by Zuili et al. in less acidic H_2SO_4 solution [33]. This surface morphology is very stable in the potential range between H_2 evolution and the onset of Ni dissolution/passivation. In particular, even on the timescale of hours neither changes in the size and number of pits nor in the shape of the steps occur, indicating the absence of significant Ni mass transport across the terraces or between the Ni surface and the electrolyte as well as a rather low mobility of Ni atoms along the step edges. Consequently, the characteristic morphological features found in the electrochemical environment, especially the monolayer deep pits, do not result from corrosion reactions, but have to result from the sample preparation procedure.

Most probably, the pits originate from long-range Ni mass transport during the formation of the NiO film in air and its subsequent reduction. Because of the different Ni density in NiO and metallic Ni (see above), the oxidation/reduction involves substantial structural rearrangement of the topmost atomic layers. It is likely that due to statistic fluctuations the defect-free Ni surface expected after annealing is not perfectly restored during this process, resulting in the formation of surface defects, such as pits. The absence of Ni islands on the terraces in most of the experiments as well as the rough terrace edges can be rationalized by a preferential reattachment of excess Ni atoms along the Ni steps. Furthermore, dissolution of minute amounts of Ni into the electrolyte during immersion (at OCP) and cathodic reduction cannot be excluded. Alternatively, the presence of the pits may be explained by the presence of impurities in the Ni bulk which segregate to the surface during annealing and are selectively dissolved upon exposure to the electrolyte. In this case, however, the coverage and density of the pits should strongly depend on the preparation conditions (such as annealing time), which was not found in the experiments.

On the atomic scale the experiments clearly indicate a Ni(111)-(1×1) lattice, confirming previous in situ STM studies [32,33,36]. In view of the high reactivity of metallic Ni strong chemisorption of species from the electrolyte solution is expected, which is supported by the reflectivity data. The observation of a (1×1) structure indicates that the adlayer is either pseudomorphic to the Ni(111) substrate, which would require a rather small adsorbate, such as H, or that the adsorbed species cannot be observed by STM because they are highly mobile on the Ni surface. Interestingly, no indication is found for the ordered sulfate '$(\sqrt{3} \times \sqrt{7})$' superstructure, which has been observed on the (111) surfaces of various fcc-metals in H_2SO_4 solution (see Ref. [70] and references therein). This might be related to two effects: First, the '$(\sqrt{3} \times \sqrt{7})$' phase is only formed positive of a critical potential, which depends on the substrate metal and which on Ni might be higher than the potential regime where the oxide-free Ni surface is stable. Second, this structure is apparently stabilized by the steric match of the sulfate tetraeder to the hexagonal (111) lattice, which might be less favorable on Ni due to the particularly small Ni lattice spacing. The presence of a strongly bound adsorbate layer, probably of an oxygen species, on reduced Ni(111) electrodes is further corrobated by the clear outward relaxation of the Ni surface layer suggested by the X-ray reflectivity experiments. The data are in excellent agreement with results obtained for Ni(111) under UHV conditions, where also a slight expansion in the presence of a (saturated) oxygen adlayer was found [77], whereas no expansion of bare [77,83] or H-covered Ni surfaces [84] was observed.

4.3. Ni dissolution

According to STM and electrochemical measurements the anodic dissolution of Ni(111) in H_2SO_4 solution commences for slow rates of potential increase at potentials between -0.25 and -0.20 V. In this case a step-flow mechanism is found in the initial stages of dissolution, in agreement with previous in situ STM studies of Ni(111) electrodes [32] and of epitaxial Ni(111) films on Ag(111) [85]. This step-flow etching proceeds isotropically with no preference of certain step orientations but not uniformly, i.e. it exhibits pronounced differences in the local dissolution rate. Possible explanations for these local variations in the step reactivity are (i) variations in the local step geometry, e.g. in the kink concentration, (ii) the local pinning of steps by passivating adsorbates, or (iii) the presence of small amounts of impurities, which accelerate dissolution (e.g. chloride). At more anodic potentials step-flow continues with higher but still nonuniform rates, resulting in an increased step roughness. A similar roughening of Ni steps was found during dissolution of ultrathin Ni(111) films on Ag(111) [85]. Parallel redeposition of the dissolving metal, as in the case of Cu(100) [72] and Cu(111) [86] dissolution in H_2SO_4, apparently does not occur during Ni dissolution. This can be attributed to the considerable hysteresis between Ni dissolution and redeposition, which suggests the presence of a kinetic barrier for this reaction, e.g. due to an inhibiting adsorbate layer on top of the Ni surface [87].

At more positive potentials the dominant mechanism for metal dissolution is the formation and growth of three-dimensional pits, i.e. dissolution occurs predominantly at specific, highly localized centers. The STM experiments clearly indicate that this mechanism, which has not been reported previously for dissolution of

(oxide-free) Ni, is not caused by selective dissolution at bulk defects, such as screw dislocations or larger inclusions. The initiation of this process at impurity atoms in the Ni surface layer can not be excluded, however, in this case the formation of monolayer deep pits rather than 3D pits would be expected. More probably, the observed 3D pitting is caused by localized dissolution in the presence of a passivating layer, a case, in which pitting corrosion is a rather common mechanism. Since the pitting occurs on an oxide-free Ni surface, only an inhibiting adsorbate layer, as also indicated otherwise by the data (see above), could account for such a passivation. In this model pitting would result from local disruption of the passivating adlayer, leading to the temporary formation of a highly active surface area. After rapid initial dissolution the pits can repassivate, either via adsorption of the inhibiting adsorbate or via local formation of the passive film. These pronounced pit growth and repassivation/activation processes result in a considerable increase in surface roughness after prolonged dissolution at higher anodic potentials.

4.4. Passive layer formation

In contrast to previous studies, where only the passive film structure after formation was probed by in situ STM [33,36], morphological changes prior to and during passive film formation on Ni(111) in 0.05 M H_2SO_4 were directly observed in this work. According to our observations the onset of passivation is preceded by rapid Ni dissolution, even if the potential is increased at a sufficiently high rate to avoid the pronounced dissolution and surface roughening described in Section 4.3. Passive layer formation proceeds via the nucleation and growth of small 3D oxide and/or hydroxide islands with a lateral size close to that of hydroxide grains observed on Ni(111) in situ on passive films [33,36] and on Ni(111) oxidized under UHV conditions [74]. Although the islands initially nucleate predominantly at steps, the surface is rapidly homogeneously covered by these islands in the further passivation process, either due to homogeneous nucleation on terraces or due to heterogeneous nucleation at additional steps, formed in the Ni dissolution process. Preferential nucleation at steps was also found in UHV–STM studies on Ni(100) oxidation [75,88], whereas homogeneous oxide nucleation was suggested in studies of Ni(111) [74] and Al(111) [89] gasphase oxidation.

At constant potential the oxide/hydroxide islands apparently grow and, in parallel, the initial, grain-like morphology is gradually transformed into a topography with sharp, oriented step edges, indicating a structural rearrangement of the passive layer. Previously such stepped morphologies were assigned to tilted, crystalline NiO grains on the Ni(111) substrate [32,33,36,48,49], which apparently form the inner part of the passive layer under steady-state conditions (see Section 4.5). Following the interpretation of Marcus and coworkers these observations suggest that passivation of Ni(111) commences by the rapid formation of a Ni hydroxide and/or hydrated oxide, followed by conversion of this phase (on a timescale of minutes) to a structural well-defined crystalline NiO layer. A similar mechanism for passivation of Ni in H_2SO_4 solution was proposed by Arvia and co-workers based on electrochemical results [28]. The fast drop of the anodic current, observed parallel to the formation of the grainy morphology in the STM experiments, indicates that already this initial phase, which can be regarded as a precursor of the crystalline passive film, hinders further dissolution, i.e. exhibits passivating properties.

The present data do not allow to distinguish unambiguously whether the passive film is formed via direct growth on the metal surface due to reactions of Ni surface atoms with solution species, similar as in gasphase oxidation reactions, or via a precipitation mechanism, where the film (or a precursor of it) is formed by precipitation of salts from the solution. On the one hand, precipitation, i.e. a genuine wet-chemical mechanism, seems possible, since the pronounced Ni dissolution observed directly prior to passivation should result in high Ni^{2+} concentrations in the near-surface region of the electrolyte. In this case, the structural differences between the passive film and the air-formed oxide (see below) could be rationalized by the differences in the formation mechanism. On the other hand, the observed surface morphology resembles that of Ni(111) surfaces oxidized under UHV conditions [74], suggesting a similar (i.e. direct growth) mechanism. For this type of growth two distinctly different mechanisms were suggested in previous studies of gasphase oxidation: For Ni(100) the heterogeneous oxide nucleation at steps is strongly preferred to homogeneous nucleation on the terraces, which are covered by a chemisorbed $c(2 \times 2)O$ adlayer [88,90], and the oxide formation proceeds via lateral growth of the nuclei. Here a transformation from O_{ad} covered Ni into the oxide at the interface between those surface phases was suggested [88]. In contrast, for Al(111) continuous homogeneous nucleation of oxide nuclei on terraces was reported [89]. In this case, it was suggested that bare and O_{ad} covered areas coexist with the surface oxide, that oxide nuclei are formed at the interface of O_{ad} islands and bare surface, and that further oxidation progresses by nucleation of additional oxide nuclei/grains rather than by growth of existing ones [89]. Due to the pronounced dissolution accompanying the passivation process we can not distinguish between these mechanisms on the basis of the present data.

4.5. Passive layer structure

The results of our in situ STM and SXS study support the duplex model of the passive film on Ni, suggested previously [29,33,36,39,41]. According to this model, which is illustrated schematically in Fig. 12a, the passive film consists of a dense, inner layer of crystalline NiO, which largely determines the corrosion properties of the passivated metal, covered by a porous outer layer of (probably amorphous) Ni hydroxide. The crystalline, inner layer exhibits a well-defined structure and thickness, which seems to depend only on the potential, whereas the structurally less defined outer layer apparently depends on the sample history, e.g. on the state of the surface (reduced or oxidized) prior to passivation. In the following we will discuss in more detail the lattice structure and orientation of the inner NiO layer, the nature of the outer part of the passive film, the structure of defects in the NiO film, and the passive film thickness.

The crystalline phase corresponds to an epitaxial NiO(111) layer which is aligned to the Ni(111) substrate. Despite the similarity in crystal structure with that of the air-formed oxide film (see Section 4.1), two distinct structural differences between the latter and the passive layer exist: First, the passive film exhibits a defined anti-parallel orientation with respect to the substrate (Fig. 12b, left) [51,63–65] and, second, the lattice of the passive oxide is slightly tilted relative to the Ni substrate [32,33,36,48,49,51]. Similar tilted oxide grains were also found for oxide films formed under UHV conditions on Ni(100) [75]. Various models have been proposed to explain this tilt and attributed it alternatively to (i) a lowering of the oxide surface energy [49], (ii) an improved epitaxial match between oxide and metal substrate lattice [48,49,75], or (iii) microscopic roughness of the oxide/metal interface, resulting from the kinetics of oxide growth [75]. The first model is based on the fact that an (unreconstructed) (111) surface of clean NiO is polar and therefore energetically unstable [91]. For a tilted oxide, in contrast, an equal number of small Ni- and O-terminated facets can coexist, resulting in an effectively unpolar surface with lower surface energy [49]. For oxide films formed in an aqueous solution, where the oxide surface energy can be minimized by an OH termination, this explanation seems rather unlikely. Second, epitaxial growth of a tilted phase may be favored by the large lattice mismatch between Ni and NiO. This was originally suggested to explain the average tilt angle of 8° found in the ex situ STM experiments on the passive film structure on Ni(111) [48,49]. The broad distribution of tilt angles found in the more recent in situ STM [33,36] and SXS [51] studies, however, seems to be at variance with a well-defined epitaxial orientation. Furthermore, the rather small average tilt angles would correspond to a good lattice match only every ~60 Å, which would imply an (energetically unfavorable) very open arrangement at the NiO/Ni interface. Finally, in this case a tilted lattice would also be expected for the air-formed oxide, contrary to the experimental data. We hence favor the third explanation, where the tilt of the oxide is rationalized by a growth of oxide grains across steps of the Ni substrate (as illustrated schematically in Fig. 12a) resulting in local distortions and tilts of the oxide lattice [75]. This model would explain the broad distribution of tilt angles by local variations in the topography. Due to the small lateral grain size, a height difference of only one to two Ni monolayers (i.e. NiO growth across one to two Ni monolayer steps) between opposite edges of the oxide grain could account for the distribution of tilt angles determined from the SXS and STM data. This also would hold true for the (more realistic) case that the atoms at the interface and in the oxide film locally relax into a configuration where the local gaps at the Ni/NiO interface are minimized. In view of the pronounced Ni dissolution and surface roughening accompanying the passive film formation, the oxide/metal interface may well exhibit a corresponding roughness. In addition, the preferred heterogeneous nucleation of oxide grains at Ni steps should further enhance the probability for oxide growth across steps. The structural differences to the untilted air-formed oxide may be caused by pronounced differences in the oxidation mechanism in the two different environments, in particular the involvement of Ni dissolution and (potentially) Ni oxide/hydroxide precipitation in the process of passive film formation (see Section 4.4).

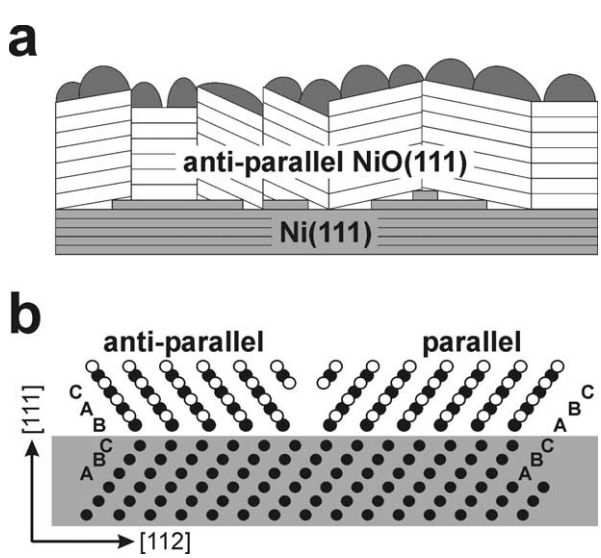

Fig. 12. (a) Structural model of the passive film formed on Ni(111) in H_2SO_4 solution, showing the Ni substrate (light gray), the crystalline NiO(111) layer (white), and the outer Ni hydroxide grains (dark gray); vertical lines indicate oxide grain boundaries (details are given in the text). (b) Schematic representation of antiparallel (left) and parallel (right) oriented NiO domains, as well as of a noncoherent twin-domain boundary between these oxide domains.

Close to the oxide/electrolyte interface the passive film and the oxide film formed by exposure to oxygen under UHV conditions should differ even more strongly. Since the latter has been shown to hydroxylate at the surface in the presence of water vapor [74,76] (partial) hydration and/or hydroxylation of the NiO film is also expected in the case of the passive film. This might explain the surface-normal lattice expansion with respect to bulk NiO(111) measured by SXS. A similar expansion of the surface-normal spacing upon incorporation of water was reported in a SXS study of $Ni(OH)_2$ [92]. According to the combined results of the STM experiments presented here and elsewhere [33,36], which indicate a well-ordered crystalline surface lattice, and the SXS experiments, where no indication for crystalline phases with in-plane lattice parameters other than those of NiO was found, this hydration/hydroxylation does not change the lateral interatomic distances in the topmost layers of the passive film relative to that of the underlying (bulklike) NiO spacing. Apparently, the rather low lattice mismatch between the close-packed (0001) plane of hexagonal $Ni(OH)_2$ and the NiO(111) plane allows accommodation of the hydrated/hydroxylated layers to those of the inner NiO lattice, i.e. a pseudomorphic arrangement. In addition, the in situ STM experiments indicate the presence of grains on top of this crystalline film, which may be associated with an apparently amorphous (and probably even more strongly hydrated/hydroxylated) Ni hydroxide phase. This phase may form either directly from the crystalline film via disruption of the topmost NiO layers due to pronounced incorporation of OH and/or H_2O or by precipitation of Ni, previously dissolved at defects in the film (see below).

The small lateral domain size of the passive oxide implies a high number of grain boundaries between the crystallites, which may strongly affect the stability of the passivated electrode. Due to the well-defined stacking sequence (i.e. the presence of only antiparallel oriented NiO), twin boundaries along the surface-normal, which have been proposed as particular easy channels of diffusion through the film [64] (see below), are not present in the passive film. The incommensurate nature of the oxide lattice and the broad distribution of tilt angles imply a high density of translational and small angle boundaries between oxide grains, however, those still allow dense packing at the grain boundary and hence should not significantly enhance the transport processes through the film. The difference in the defect structure may, in addition to the larger oxide thickness, explain the higher stability against cathodic oxide reduction and open circuit breakdown of the passive film as compared with the air-formed oxide, found previously in electrochemical experiments [26].

In the regime of passivity (0.10–0.80 V in 0.05 M H_2SO_4) the electrode potential primarily affects the thickness of the oxide layer. In contrast to previous studies by ex situ XPS [29,33,36,41] and in situ ellipsometry [8,46], the SXS experiments directly and exclusively measure the thickness of the crystalline, inner NiO layer, whereas they are insensitive to the more porous, outer part of the passive film. The data clearly confirm that the thickness of the inner layer increases approximately linearly with potential. The absolute values of the thickness, its dependence on potential (14–17 Å V^{-1}), and the shift of the thickness curves with solution pH ($\sim$60 mV), are in good agreement with the previous results [29,33,36,41]. Furthermore, for passivation of reduced samples the SXS experiments suggest a decrease in grain size with increasing potential. This can be attributed to an increase in the nucleation density of oxide crystallites as also found in previous studies [49], reflecting the higher driving force towards oxide formation.

4.6. Oxide-covered Ni(111) surfaces after immersion

According to our SXS study, the air-formed oxide on Ni(111) changes significantly after direct immersion into 0.05 M H_2SO_4 at potentials in the passive range, resulting after prolonged exposure to the solution in an oxide film with an apparently identical structure as the passive oxide formed on previously reduced samples. These changes can not be explained by a direct restructuring of the oxide grains, since a conversion from parallel to antiparallel oxide or from untilted to tilted oxide would require substantial collective mass transport. More likely, the continuous dissolution and reformation of the oxide film in the passive range, indicated by previous radiotracer studies [52,53], causes the replacement of the initial air-formed oxide by the (steady-state) passive film.

The in situ STM experiments show that this transition is accompanied by substantial morphological changes. On short time scales (up to 1 h) the smooth topography of the initial oxide is largely maintained, indicating that pronounced active dissolution is effectively blocked by the air-formed oxide. Only localized dissolution, resulting in the formation of nanometer-sized pits, occurs, which is attributed to NiO dissolution at defect sites of the air-formed oxide. As noted above, the coexistence of parallel and anti-parallel oxide domains in the air-formed oxide implies the presence of incoherent twin boundaries between the oxide grains (see Fig. 12b), where mass transport through the film should be markedly more facile and which therefore should act as preferred sites of dissolution [10,64,93]. This is supported by the predominant occurrence of pits along steps, i.e. at the probable location of grain boundaries. Upon longer immersion at passive potentials, the surface gradually roughens and develops a 'grainy' appearance, similar to that observed directly (within several

seconds) after passivation of reduced samples. Following Zuili et al. [33,36,33,36], the formation of this morphology can be rationalized by the slow formation of a hydroxide and/or hydrated oxide layer on top of the crystalline oxide. The direct growth or precipitation of this hydroxide layer requires the presence of Ni ions at the electrolyte/NiO interface. In contrast to the passivation of reduced Ni surfaces, where considerable amounts of these Ni ions are generated due to the pronounced, parallel dissolution of the (metallic) Ni electrode, the dissolution of Ni surfaces covered by the air-formed oxide can only proceed at defects in the oxide film and hence is significantly slower. This explains the much slower formation of the hydroxide layer in the latter case.

As a consequence of the structural conversion of the initially highly defective air-formed oxide film, the corrosion rate should gradually decrease after longer immersion and finally approach that of passive oxides formed on reduced samples. Upon reemersion from the 0.05 M H_2SO_4 solution these changes are partially reversed, resulting in the reemergence of parallel oriented NiO grains. Possible explanations for the latter are (i) a direct conversion of the oxide due to dehydration and/or dehydroxylation processes and/or (ii) the (partial) dissolution of the passive film, followed by oxide reformation in air during the emersion and transfer procedure. In the latter case the dissolution processes can be attributed to chemical dissolution of the oxide in the acidic solution after the potential control is released, an effect which is expected in particular in strongly acidic electrolytes [4]. The far lower diffracted intensity after emersion probably reflects a less defined oxide structure, e.g. a broader distribution of tilt or rotation angles, and/or a higher roughness on the atomic scale, as also supported by EXAFS results on passivated and emersed Ni electrodes [50]. Such structural changes during immersion/emersion can be expected to influence the atmospheric corrosion of Ni. Due to the reappearance of the mixed parallel/antiparallel oxide new defects, such as twin boundaries, are created upon emersion which may exhibit an enhanced reactivity for corrosion reactions after reimmersion into the electrolyte. This would cause an increased corrosion rate in dry–wet cycles, i.e. under conditions common in outdoor atmospheric corrosion.

5. Conclusions

We have presented a detailed in situ/ex situ STM, SXS, and electrochemical study of the structure and morphology of Ni(111) surfaces in air and in H_2SO_4 solution and of the mechanisms of Ni dissolution and oxide formation. The major results are:

- In agreement with previous studies, structurally well-defined Ni surfaces can be prepared by annealing in H_2 atmosphere and subsequent exposure to air at room temperature. The resulting surface is covered by a three to four layers thick, (111)-oriented NiO film, consisting of untilted, parallel (NiO[$1\bar{1}0$]||Ni[$1\bar{1}0$]) and anti-parallel (NiO[$1\bar{1}0$]||Ni[$1\bar{1}0$]) oriented oxide grains.
- Upon immersion into 0.05 M H_2SO_4 solution at potentials ≤ -0.40 V the air-formed oxide is reduced, resulting in atomically smooth, oxide-free Ni electrode surfaces with very low surface mobility. The experiments indicate the presence of a (1×1) or disordered, chemisorbed adlayer, most probably an O/OH or anion species, which induces an outward relaxation of the Ni surface atoms. The occurrence of monolayer deep pits on the reduced Ni surface is proposed to result from mass transport processes during the (air) oxidation and the subsequent electrochemical reduction.
- Dissolution of the oxide-free Ni surface in 0.05 M H_2SO_4 commences at -0.25 to -0.20 V via a step flow mechanism. At more positive potentials Ni dissolves with higher rates and predominantly by the formation and growth of three-dimensional pits. This pitting is tentatively attributed to the presence of an inhibiting adlayer, which is locally removed. Due to the formation and (re-) passivation of such etch pits the Ni surface roughness increases substantially during dissolution.
- In situ STM observations of the passive film formation on reduced surfaces show a rapid nucleation and growth process, followed by slower restructuring of the oxide film. This can be rationalized by a two-step process, where an initial hydroxide/hydrated oxide phase is converted into NiO.
- Structural studies of the passive film formed at potentials ≥ -0.10 to 0.00 V (depending on the rate of potential increase) support the duplex model of the passive film, suggested previously, with a dense, crystalline inner layer, consisting of an exclusively anti-parallel oriented NiO(111) film, and a more porous (probably amorphous) outer layer of Ni hydroxide. The NiO grains exhibit a small-angle tilt relative to the Ni substrate with a broad distribution of tilt angles, which is tentatively attributed to the oxide growth kinetics. A surface-normal expansion of the NiO lattice suggests partial hydration/hydroxylation of the inner layer. From the SXS measurements a potential-dependent thickness of the inner crystalline layer of 10–20 Å is deduced in the potential range from 0.30 to 0.80 V, with slopes of 14–17 Å V^{-1}.
- Upon immersion of Ni samples at potentials in the passive range the air-formed oxide is first dissolved locally, which is attributed to the presence of twin-domain boundaries between the oxide grains. On

longer time scales the air-formed oxide is gradually transformed into the passive film, most likely by (slow) continuous dissolution and reformation processes. Structural and morphological changes also occur after emersion of the samples from the electrolyte, most likely by partial dissolution of the passive film and reoxidation in air as well as by dehydration or dehydroxylation processes. Such effects may affect the corrosion resistance of Ni under outdoor atmospheric corrosion conditions.

Acknowledgements

We gratefully acknowledge financial support and a fellowship for O.M.M. by the Deutsche Forschungsgemeinschaft. Brookhaven National Laboratory is supported by the Department of Energy under Contract No. DE-AC-02-98CH10886. Also we would like to thank R.J. Behm and P. Marcus for interesting discussions.

References

[1] J.W. Schultze, M.M. Lohrengel, Electrochim. Acta 45 (2000) 2499.
[2] A.J. Arvia, D. Posadas, in: A.J. Bard (Ed.), Encyclopedia of Electrochemistry of the Elements, Marcel Dekker, New York, 1975, p. 211.
[3] N. Sato, G. Okamoto, in: J.O. Bockris, B.E. Conway, E. Yeager, R.E. White (Eds.), Electrochemical Materials Science, vol. 4, Plenum Press, New York, 1981, p. 193.
[4] B. MacDougall, M.J. Graham, in: P. Marcus, J. Oudar (Eds.), Corrosion Mechanisms in Theory and Practice, Marcel Dekker, New York, 1995, p. 143.
[5] C.R. Brundle, J.Q. Brougthon, in: D.A. King, D.P. Woodruff (Eds.), The Initial Interaction of Oxygen with Well-defined Transition Metal Surfaces. Chemisorption Systems, Part A, vol. 3, Elsevier, Amsterdam, 1990, pp. 131–388.
[6] F. Besenbacher, J.K. Norskov, Prog. Surf. Sci. 44 (1993) 5.
[7] K.J. Vetter, K. Arnold, Z. Elektrochem. 64 (1960) 244.
[8] J.O. Bockris, A.K.N. Reddy, B. Rao, J. Electrochem. Soc. 113 (1966) 1133.
[9] R.L. Cowan, R.W. Staehle, J. Electrochem. Soc. 118 (1971) 557.
[10] R.M. Latanision, H. Opperhauser, Corrosion 27 (1971) 509.
[11] H. Gobrecht, W. Paatsch, R. Thull, Ber. Bunsenges. Phys. Chem. 75 (1971) 1353.
[12] H.G. Feller, H.-J. Rätzer-Scheibe, W. Wendt, Electrochim. Acta 17 (1972) 187.
[13] A. Jouanneau, M. Keddam, M.C. Petit, Electrochim. Acta 21 (1976) 287.
[14] A. Jouanneau, M.-C. Petit, J. Chim. Phys. 73 (1976) 82.
[15] M. Zamin, M.B. Ives, J. Electrochem. Soc. 126 (1979) 470.
[16] J. Oudar, P. Marcus, Appl. Surf. Sci. 3 (1979) 48.
[17] B. MacDougall, D.F. Mitchell, M.J. Graham, Corrosion 38 (1982) 85.
[18] M. Keddam, H. Takenouti, N. Yu, J. Electrochem. Soc. 132 (1985) 2561.
[19] M. Keddam, H. Takenouti, N. Yu, Corros. Sci. 27 (1987) 107.
[20] R.J. Smith, R.E. Hummel, J.R. Ambrose, Corros. Sci. 27 (1987) 815.
[21] B. MacDougall, M. Cohen, J. Electrochem. Soc. 122 (1975) 383.
[22] B. MacDougall, M. Cohen, J. Electrochem. Soc. 123 (1976) 191.
[23] B. MacDougall, M. Cohen, J. Electrochem. Soc. 123 (1976) 1783.
[24] J.R. Vilche, A.J. Arvia, J. Electrochem. Soc. 123 (1976) 1061.
[25] J.R. Vilche, A.J. Arvia, Corros. Sci. 18 (1978) 441.
[26] B. MacDougall, D.F. Mitchell, M.J. Graham, Isr. J. Chem. 18 (1979) 125.
[27] S.G. Real, J.R. Vilche, A.J. Arvia, Corros. Sci. 20 (1980) 563.
[28] M.R. Barbosa, S.G. Real, J.R. Vilche, A.J. Arvia, J. Electrochem. Soc. 135 (1988) 1077.
[29] H.-W. Hoppe, H.-H. Strehblow, Corros. Sci. 31 (1990) 167.
[30] G. Larramona, C. Gutierrez, J. Electrochem. Soc. 137 (1990) 428.
[31] C.F. Zinola, A.M. Castro Luna, Corros. Sci. 37 (1919) 1995.
[32] T. Suzuki, T. Yamada, K. Itaya, J. Phys. Chem. 100 (1996) 8954.
[33] P. Natishan, H.S. Isaacs, M. Janik-Czachor, et al. (Eds.), In Situ Investigation by ECSTM of the Structure of the Passive Film Formed on Ni(111) Single-Crystal Surfaces. Passivity and Its Breakdown, vols. PV 97-26, The Electrochemical Society, Pennington, NJ, 1997, pp. 1013–1024.
[34] A. Cuesta, C. Gutierrez, Langmuir 14 (1998) 3397.
[35] V. Maurice, V. Inard, P. Marcus, Electrochem. Soc. Proc. 98–17 (1999) 552.
[36] D. Zuili, V. Maurice, P. Marcus, J. Electrochem. Soc. 147 (2000) 1393.
[37] M. Keddam, in: P. Marcus, J. Oudar (Eds.), Corrosion Mechanisms in Theory and Practice, Marcel Dekker, New-York, 1995, p. 55.
[38] T. Dickinson, A.F. Povey, P.M.A. Sherwood, J. Chem. Soc. Faraday Trans. I 73 (1977) 327.
[39] P. Marcus, J. Oudar, I. Olefjord, J. Microsc. Spectrosc. Electron. 4 (1979) 63.
[40] R.E. Hummel, R.J. Smith, E.D. Verink, Corros. Sci. 27 (1987) 803.
[41] H.-W. Hoppe, H.-H. Strehblow, Surf. Interf. Anal. 14 (1989) 121.
[42] P. Marcus, J.-M. Herbelin, Corros. Sci. 34 (1993) 1123.
[43] D.F. Mitchell, G.I. Sproule, M.J. Graham, Appl. Surf. Sci. 21 (1985) 199.
[44] P. Delichere, A. Hugot-Le Goff, N. Yu, J. Electrochem. Soc. 133 (1986) 2106.
[45] T. Ohtsuka, K. Schoner, K.E. Heusler, J. Electroanal. Chem. 93 (1978) 171.
[46] Y. Kang, W. Paik, Surf. Sci. 182 (1987) 257.
[47] B. MacDougall, M. Cohen, J. Electrochem. Soc. 121 (1974) 1152.
[48] V. Maurice, H. Talah, P. Marcus, Surf. Sci. 284 (1993) L431.
[49] V. Maurice, H. Talah, P. Marcus, Surf. Sci. 304 (1994) 98.
[50] R. Cortes, M. Froment, A. Hugot-Le Goff, S. Joiret, Corros. Sci. 31 (1990) 121.
[51] O.M. Magnussen, J. Scherer, B.M. Ocko, R.J. Behm, J. Phys. Chem. B 104 (2000) 1222.
[52] J. Siejka, C. Cherki, J. Yahalom, J. Electrochem. Soc. 119 (1972) 991.
[53] B. MacDougall, D.F. Mitchell, M.J. Graham, J. Electrochem. Soc. 132 (1985) 2895.
[54] B. MacDougall, M. Cohen, J. Electrochem. Soc. 124 (1977) 1185.
[55] B. MacDougall, M. Cohen, Electrochim. Acta 23 (1978) 145.
[56] B. MacDougall, J. Electrochem. Soc. 125 (1883) 1978.
[57] B. MacDougall, J. Electrochem. Soc. 130 (1983) 114.
[58] O. Lev, F.-R. Fan, A.J. Bard, J. Electrochem. Soc. 135 (1988) 783.
[59] S. Ando, T. Suzuki, K. Itaya, J. Electroanal. Chem. 412 (1996) 139.
[60] P. Müller, S. Ando, T. Yamada, K. Itaya, J. Electroanal. Chem. 467 (1999) 282.
[61] J. Wiechers, T. Twomey, D.M. Kolb, R.J. Behm, J. Electroanal. Chem. 248 (1988) 451.
[62] J. Wang, B.M. Ocko, A.J. Davenport, H.S. Isaacs, Phys. Rev. B 46 (1992) 10321.

[63] K.R. Lawless, F.W. Young, A.T. Gwathmey, J. Chim. Phys. 53 (1956) 667.
[64] J.V. Cathcart, G.F. Petersen, C.J. Sparks, J. Electrochem. Soc. 116 (1969) 664.
[65] M.J. Graham, R.J. Hussey, M. Cohen, J. Electrochem. Soc. 120 (1973) 1523.
[66] O.M. Magnussen, J. Hageböck, J. Hotlos, R.J. Behm, Faraday Discuss. 94 (1992) 329.
[67] G.J. Edens, X. Gao, M.J. Weaver, J. Electroanal. Chem. 375 (1994) 357.
[68] A.M. Funtikov, U. Linke, U. Stimming, R. Vogel, Surf. Sci. 324 (1995) L343.
[69] L.-J. Wan, S.-L. Yau, K. Itaya, J. Phys. Chem. 99 (1995) 9507.
[70] M. Wilms, P. Broekmann, C. Stuhlmann, K. Wandelt, Surf. Sci. 416 (1998) 121.
[71] L.-J. Wan, M. Hara, J. Inukai, K. Itaya, J. Phys. Chem. B 103 (1999) 6978.
[72] M.R. Vogt, A. Lachenwitzer, O.M. Magnussen, R.J. Behm, Surf. Sci. 399 (1998) 49.
[73] M.F. Toney, J.N. Howard, J. Richer, G.L. Borges, J.G. Gordon, O.R. Melroy, D.G. Wiesler, D. Yee, et al., Nature 368 (1994) 444.
[74] N. Kitakatsu, V. Maurice, C. Hinnen, P. Marcus, Surf. Sci. 407 (1998) 36.
[75] M. Bäumer, D. Cappus, H. Kuhlenbeck, H.-J. Freund, G. Wilhelmi, A. Brodde, H. Neddermeyer, Surf. Sci. 253 (1991) 116.
[76] P.R. Norton, R.L. Tapping, J.W. Goodale, Surf. Sci. 65 (1977) 13.
[77] T. Narusawa, W.M. Gibson, E. Törnquist, Phys. Rev. Lett. 47 (1981) 417.
[78] T. Narusawa, W.M. Gibson, E. Törnquist, Surf. Sci. 114 (1982) 331.
[79] D. Cappus, C. Xu, D. Ehrlich, B. Dillmann, C.A. Ventrice, K. Al Shamery, H. Kuhlenbeck, H.-J. Freund, Chem. Phys. 177 (1993) 533.
[80] C.A. Ventrice, T. Bertrams, H. Hannemann, A. Brodde, H. Neddermeyer, Phys. Rev. B 49 (1994) 5773.
[81] M.A. Langell, C.L. Berrie, M.H. Nassir, K.W. Wulser, Surf. Sci. 320 (1994) 25.
[82] M.A. Langell, M.H. Nassir, J. Phys. Chem. 99 (1995) 4162.
[83] R.C. Bhardwaj, A. Gonzalez-Martin, J.O. Bockris, J. Electrochem. Soc. 138 (1901) 1991.
[84] L. Hammer, H. Landskron, W. Nichtl-Pecher, A. Fricke, K. Heinz, K. Müller, Phys. Rev. B 47 (1993) 15969.
[85] A. Lachenwitzer, Ph.D., Universität Ulm, 2000.
[86] W. Polewska, M.R. Vogt, O.M. Magnussen, R.J. Behm, J. Phys. Chem. B 103 (1999) 10440.
[87] A. Lachenwitzer, O.M. Magnussen, J. Phys. Chem. B 104 (2000) 7424.
[88] E. Kopatzki, R.J. Behm, Phys. Rev. Lett. 74 (1995) 1399.
[89] H. Brune, J. Wintterlin, J. Trost, G. Ertl, J. Wiechers, R.J. Behm, J. Chem. Phys. 99 (1993) 2128.
[90] E. Kopatzki, Ph.D., Ludwig-Maximilians-Universität, München, 1994.
[91] D. Wolf, Phys. Rev. Lett. 68 (1992) 3315.
[92] D. Singh, J. Electrochem. Soc. 145 (1998) 116.
[93] C.J. Mauvais, R.M. Latanision, A.W. Ruff, J. Electrochem. Soc. 117 (1970) 902.